



Universiteit
Leiden
The Netherlands

Josephson and noise scanning tunneling microscopy on conventional, unconventional and disordered superconductors

Chatzopoulos, D.

Citation

Chatzopoulos, D. (2021, November 25). *Josephson and noise scanning tunneling microscopy on conventional, unconventional and disordered superconductors*. *Casimir PhD Series*. Retrieved from <https://hdl.handle.net/1887/3243474>

Version: Publisher's Version

License: [Licence agreement concerning inclusion of doctoral thesis in the Institutional Repository of the University of Leiden](#)

Downloaded from: <https://hdl.handle.net/1887/3243474>

Note: To cite this publication please use the final published version (if applicable).

A

Appendix: Inhomogeneous superfluid density in Fe(Te,Se)

A.1. Sample preparation and measurement

$\text{FeTe}_x\text{Se}_{1-x}$ single crystals with an optimal concentration of $x = 0.55$ are grown by the Bridgman method. The magnetic susceptibility curve as a function of temperature shows a sharp transition at $T_C \approx 14.5$ K. To perform STM and scanning tunnelling spectroscopy measurements, we use a modified commercial scanning tunnelling microscope (USM-1500, Unisoku Co., Ltd). The samples are cleaved in ultrahigh vacuum (base pressure, $p_{\text{base}} \approx 1 \times 10^{-10}$ mbar) at low temperature ($T \approx 30$ K) and are immediately mounted in the pre-cooled STM head ($T \approx 2.2$ K) to prevent surface reconstruction and contamination. Mechanically grinded Pt–Ir wires are used as STM tips. To make a superconducting tip, we indent the metallic tip into a Pb(111) surface cleaned by repeated sputtering and annealing. The STM topographs in Fig. 3.2a (Fig. 3.3a) are acquired by a constant current mode with $V_{\text{set}} = -10$ mV (+6 mV) and $I_{\text{set}} = 5.0$ nA (0.12 nA). A standard lock-in technique is employed for the tunnelling spectrum measurements. We apply a voltage modulation of 0.1–0.2 mV for the quasiparticle tunnelling spectra (Figs. 3.3d–f) and 0.01–0.02 mV for the Josephson tunnelling spectra (Figs. 3.2c, 3.3b) with a frequency of 887 Hz. The former is obtained with $V_{\text{set}} = -6$ mV and $I_{\text{set}} = 0.3$ nA and the latter with $V_{\text{set}} = -6$ mV and $I_{\text{set}} = 5$ nA. All measurements reported are performed at 2.2 K.

A.2. Critical current as a function of normal-state conductance

The superconducting tip prepared on Pb is used on $\text{FeTe}_{0.55}\text{Se}_{0.45}$. Fig. A.1a, b shows the R_N -dependent I - V curves. We observe that for decreasing R_N , the current reaches a maximum value at finite bias around the Fermi level, which is an indication of Cooper pair tunnelling. In the differential conductance spectra shown in Fig. A.1c, d, we can resolve sharp resonances at finite bias originating from the energy exchange between Cooper pairs and the electromagnetic environment of the junction.

According to the IZ model, the maximum (I_{max}) in the I - V characteristic curves is related to the critical supercurrent according to the formula

$$I_C = \sqrt{\frac{8I_{\text{max}}ek_B T}{\hbar}}. \quad (\text{A.1})$$

Hence, we can use the maximum from our I - V curves and use the above formula for quantifying I_C (we use $T = 2.2$ K, which is equal to our measurement temperature). In Fig. A.1e, we plot I_C as function of the normal-state junction conductance, $G_N = 1/R_N$. A linear trend is observed, which is consistent with the so-called Ambegaokar–Baratoff formula [1]. A linear fit to our data gives a slope of 1.534 meV, which is used to estimate $\Delta_{\text{CP},s}$ from the formula of an asymmetric junction [2]

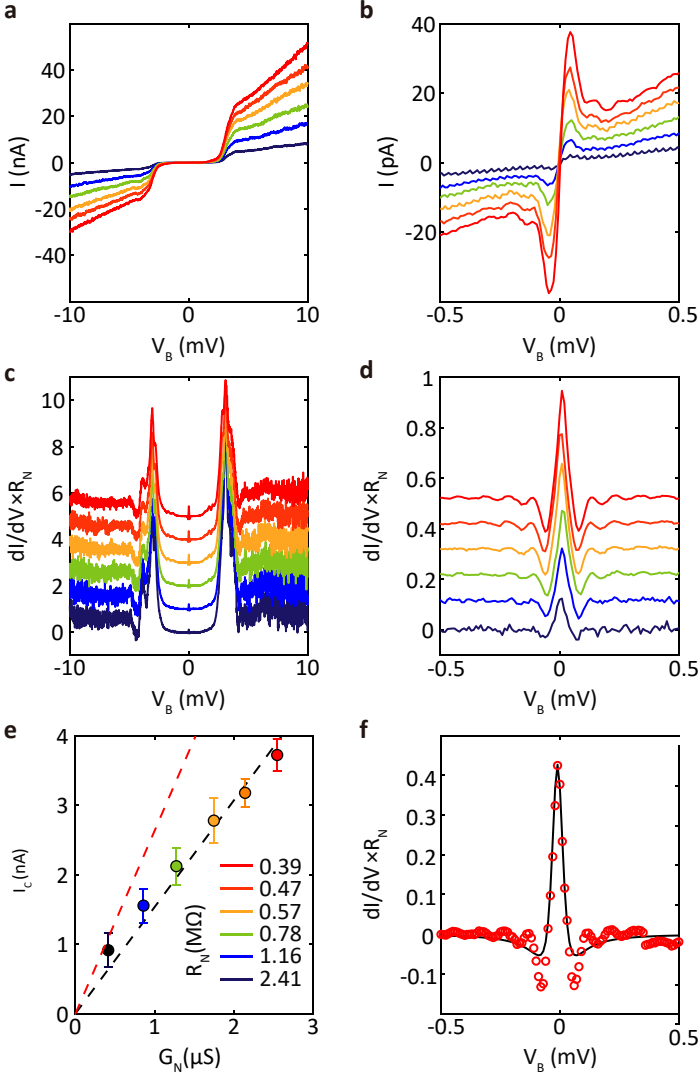


Figure A.1: **Josephson tunnelling spectroscopy in a Pb/Fe(Te,Se) junction.** **a,b** R_N -dependent I - V curves (see key in **e**). **c,d** Corresponding R_N -dependent dI/dV curves, multiplied by R_N . The datasets are offset for clarity. For decreasing R_N , the zero-bias peak and the small modulations (with a period of 0.1 meV) induced by Cooper pair tunnelling become more pronounced. **e** Linear relation (black dashed line) between the critical Josephson current I_C and the normal-state conductance, G_N . Each point is the average of 20 points extracted from 20 I - V curves, as described in the main text. For each R_N , we also extract the standard deviation of I_{\max} and obtain the error bars shown in the figure by performing error propagation via the IZ formula. The red dashed line corresponds to the AB formula for a asymmetry Josephson junction in which two superconductor electrodes have the same s -wave symmetry with different pair-breaking gaps ($\Delta_{\text{CP,t}} = 1.30$ meV and $\Delta_{\text{CP,s}} = 1.68$ meV). **f** Fitting (black curve) of a normalized conductance spectrum (red circles) using the IZ model. All dI/dV spectra are acquired with $V_{\text{set}} = -10$ mV and a lock-in modulation of $V_{\text{mod}} = 20$ μV peak to peak.

$$I_C R_N = \frac{2}{e} \frac{\Delta_{CP,s} \Delta_{CP,t}}{\Delta_{CP,s} + \Delta_{CP,t}} K \left(\left| \frac{\Delta_{CP,s} - \Delta_{CP,t}}{\Delta_{CP,s} + \Delta_{CP,t}} \right| \right), \quad (\text{A.2})$$

where $K(x)$ is the elliptic integral function of the first kind. Assuming that $\Delta_{CP,t} = 1.3$ meV, we find $\Delta_{CP,t} = 0.67$ meV. This is to be compared with the gap that we read from our conductance spectra. We find that the coherence peak is located at 3.08 meV. Subtracting $\Delta_{CP,t}$ from the coherence peak location gives $\Delta_{CP,s} = 1.68$ meV. We believe that this deviation can be attributed to the unconventional superconducting nature of $\text{FeTe}_{0.55}\text{Se}_{0.45}$. It has been predicted theoretically that for Cooper pair tunnelling between a conventional s -wave superconductor and an unconventional s_{\pm} multiband superconductor (here $\text{FeTe}_{0.55}\text{Se}_{0.45}$), I_C grows linearly with G_N . However, for that case the slope is expected to be lower than for the single-band, s -wave case [3–8]. A reduction in the Josephson current was also observed in a multiband superconductor without a sign-changing gap using an s -wave superconducting tip [9]. We expect that better calculations of the orbital decomposition of the gap structure and of the individual tunnelling processes for different orbitals will allow the quantitative interpretation of our data.

A.3. Effect of inhomogeneous R_N

To visualize the spatial variations of the superfluid density, we record differential conductance spectroscopic maps on a grid of points (r_x, r_y) . By taking the derivative of the IZ formula with respect to the voltage, we obtain

$$\frac{dI}{dV} = \frac{I_C^2 Z_{\text{env}}}{2} \frac{V_C^2 - V^2}{(V^2 + V_C^2)^2}. \quad (\text{A.3})$$

We fit our spectrum with the above formula using the pre-factor $I_C^2 Z_{\text{env}}/2$ and V_C as free parameters. A typical IZ fit of the conductance spectrum is shown in Fig. A.1f. This allows us to construct atomic-scale $I_C(r)$ maps, which express the magnitude of the critical supercurrent as a function of location r . Fig. A.2a, b shows examples of such maps, obtained in the same 25×25 nm² field of view and using opposite setup bias (-10 mV in Fig. A.2a and $+10$ mV in Fig. A.2b). These maps reveal spatial variations of the critical supercurrent on a small length scale of a few nanometres. However, we notice that these two maps are not consistent. This is because I_C (the measured critical current of the junction) is influenced by the single-particle tunnelling transmission rate, represented by $1/R_N$, at each point. To enable the direct measurement of intrinsic variations of the superfluid density, we take the product of the measured $I_C(r)$ with $R_N(r)$ (see ref. [10]). Fig. A.2c, d shows measured $R_N(r)$ images acquired in the same field of view as the $I_C(r)$ maps for both bias polarities. The $R_N(r)$ maps can be obtained by either:

- summing over all spatially resolved differential conductance layers $g(r)$ and dividing by the size of the energy window
- spatially mapping the tunnelling current $I(r)$ at a bias larger than the superconducting pair-breaking gap Δ_{CP} and computing $R_N(r)$ by assuming an

Ohmic relation for the single-particle tunnelling.

A

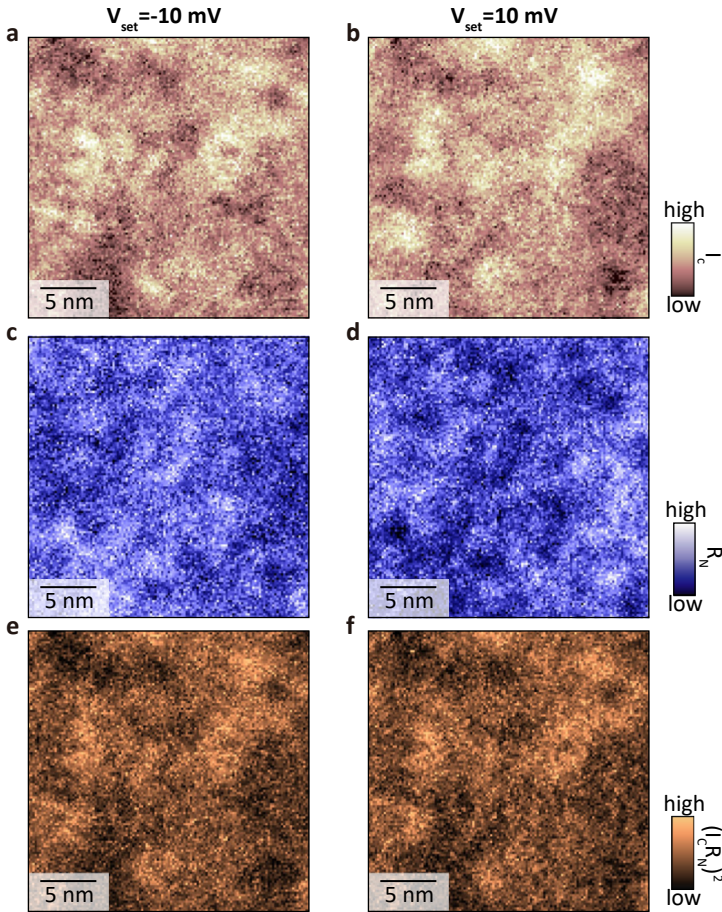


Figure A.2: **Superfluid density maps with inhomogeneous normal-state resistance.** **a, b** Maps of the critical Josephson current I_C . **c, d** Spatial variations of the normal-state resistance, R_N . **e, f** Maps of $(I_C R_N)^2$ associated with the superfluid density. The images in the left (right) column were acquired with a setup bias of -10 mV ($+10$ mV) and a setup current of 10 nA. To map the intrinsic superfluid density, it is necessary to normalize the measured I_C by multiplying with R_N . Topographs were acquired simultaneously with these measurements and used to align the different maps.

A.4. Bogoliubov quasiparticle interference

$\text{FeTe}_{0.55}\text{Se}_{0.45}$ is known to be a multiband superconductor. Similarly to other Fe-based superconductors, its normal electronic state in the **a**-**b** plane has two hole-like bands around the centre of the Brillouin zone and two electron-like bands around its corners (Fig. A.3b). The bulk band structure along the **c** axis has been predicted to have nontrivial topological invariance due to the Te substitutions [11]. High-resolution angle-resolved photoemission spectroscopy experiments demonstrated the existence of a Dirac-cone-type spin-helical surface state and its *s*-wave superconductivity [12].

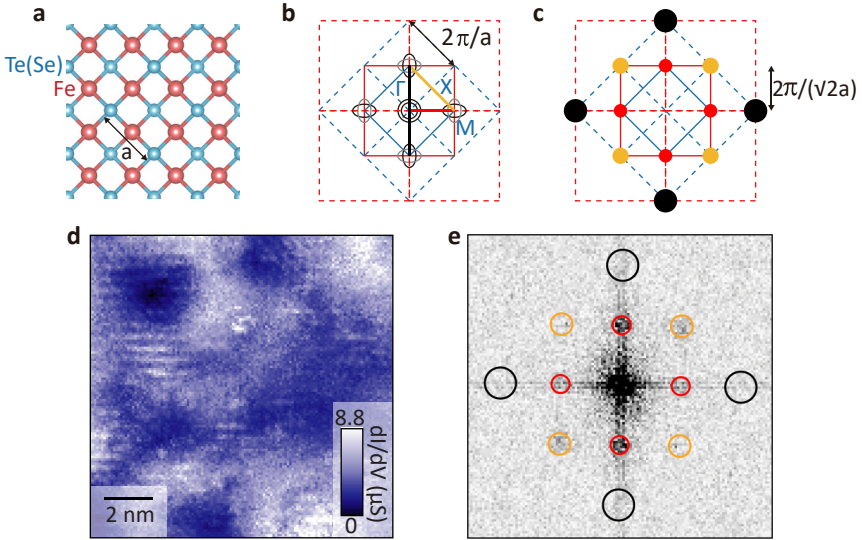


Figure A.3: **Quasiparticle interference induced by inter-pocket scattering in Fe(Te,Se)** **a** Top-view of the atomic structure of $\text{FeTe}_{0.55}\text{Se}_{0.45}$. The blue and red spheres denote the chalcogen and the transition metal atoms, respectively. **b** Fermi surface of $\text{FeTe}_{0.55}\text{Se}_{0.45}$. Two hole pockets are at the Γ point and one electron pocket at the M point, marked by black circles and ellipses. The red (blue) dashed lines correspond to the reciprocal lattice of Fe (chalcogen) layer. Because the unit cell includes two Fe atoms, the Brillouin zone of Fe (red square) atoms is two times larger than that of the full crystal structure (blue square). The alternate vertical positions of the chalcogen atoms above and below the Fe layer lead to a folded band (grey ellipse centred at the M point) composed of out-of-plane d orbitals [13]. Here we highlight the inter-pocket scattering wavevectors with black, yellow and red solid arrows. **c** Sketch of scattering wavevectors in the reciprocal lattice. The colour coding is identical to that in **b**. **d** Stripy patterns in a dI/dV map at +3.9 meV induced by inter-pocket scattering ($V_{\text{set}} = -10$ mV, $I_{\text{set}} = 20$ nA and $V_{\text{mod}} = 200$ μV peak to peak). **e** FFT spectrum of quasiparticle interference patterns. The circles correspond to the inter-pocket scattering wavevectors in **b** with the same colour coding.

Hanaguri et al.[14] reported quasi-particle inferences on Fe(Se,Te). The inter-band scattering between hole and electron pockets, highlighted by the red line and dots in Fig. A.3b, c, result in spatial modulations of the local density of states. Our dI/dV map (Fig. A.3d) and its fast Fourier transform (FFT) spectrum (Fig. A.3e) clearly show the same patterns around coherent peaks. Our FFT spectrum shows blurred (ring-like) features, marked by red circles in Fig. A.3e, with wavevectors

that correspond to the inter-pocket scattering wavevector. Because the FFT spectral feature is very sharp and is not dispersive, another interpretation of its origin is a broken symmetry ground state, such as a spin density wave or its relevant surface reconstruction [15, 16].

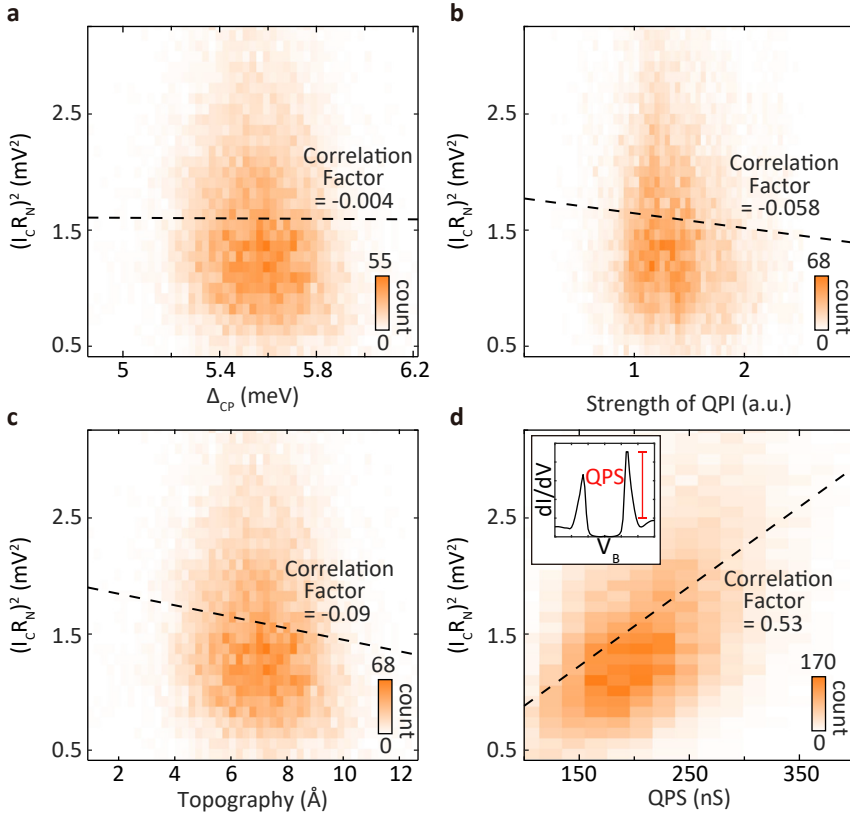


Figure A.4: **Correlation plots between superfluid density and various parameters.** **a–d** Correlation between superfluid density and pair-breaking gap (**a**); strength of quasiparticle interference (**b**); topographic height (**c**) and quasiparticle strength minus the normal-state conductance (**d**; see inset), which gives similar results to those obtained without subtracting the normal conductance, as in the main text.

References

- [1] V. Ambegaokar and A. Baratoff, *Tunneling between superconductors*, Phys. Rev. Lett. **10**, 486 (1963).
- [2] P. Anderson, *Special effects in superconductivity*, in *Lectures on the many-body problem 2* (Academic Press Inc., New York, 1964) pp. 113–135.
- [3] Y. Ota, N. Nakai, H. Nakamura, M. Machida, D. Inotani, Y. Ohashi, T. Koyama, and H. Matsumoto, *Ambegaokar-Baratoff relations for Josephson critical current in heterojunctions with multigap superconductors*, Phys. Rev. B **81**, 214511 (2010).
- [4] C. C. Tsuei and J. R. Kirtley, *Pairing symmetry in cuprate superconductors*, Rev. Mod. Phys. **72**, 969 (2000).
- [5] T. K. Ng and N. Nagaosa, *Broken time-reversal symmetry in Josephson junction involving two-band superconductors*, Europhys. Lett. **87**, 17003 (2009).
- [6] Y. Ota, M. Machida, T. Koyama, and H. Matsumoto, *Theory of Heterotic Superconductor-Insulator-Superconductor Josephson Junctions between Single- and Multiple-Gap Superconductors*, Phys. Rev. Lett. **102**, 237003 (2009).
- [7] P. Seidel, *Josephson effects in iron based superconductors*, Supercond. Sci. Tech. **24**, 043001 (2011).
- [8] S.-Z. Lin, *Josephson effect between a two-band superconductor with s_{++} or s_{\pm} pairing symmetry and a conventional s -wave superconductor*, Phys. Rev. B **86**, 014510 (2012).
- [9] O. Naaman, R. Dynes, and E. Bucher, *Josephson Effect in Pb/I/NbSe₂ Scanning Tunneling Microscope Junctions*, Int. J. Mod. Phys. B **17**, 3569 (2003).
- [10] M. Hamidian, S. Edkins, S. H. Joo, A. Kostin, H. Eisaki, S. Uchida, M. Lawler, E.-A. Kim, A. Mackenzie, K. Fujita, *et al.*, *Detection of a Cooper-pair density wave in Bi₂Sr₂CaCu₂O_{8+x}*, Nature **532**, 343 (2016).
- [11] Z. Wang, P. Zhang, G. Xu, L. K. Zeng, H. Miao, X. Xu, T. Qian, H. Weng, P. Richard, A. V. Fedorov, H. Ding, X. Dai, and Z. Fang, *Topological nature of the FeSe_{0.5}Te_{0.5} superconductor*, Phys. Rev. B **92**, 115119 (2015).
- [12] P. Zhang, K. Yaji, T. Hashimoto, Y. Ota, T. Kondo, K. Okazaki, Z. Wang, J. Wen, G. D. Gu, H. Ding, and S. Shin, *Observation of topological superconductivity on the surface of an iron-based superconductor*, Science **360**, 182 (2018).
- [13] L. Moreschini, P.-H. Lin, C.-H. Lin, W. Ku, D. Innocenti, Y. J. Chang, A. L. Walter, K. S. Kim, V. Brouet, K.-W. Yeh, M.-K. Wu, E. Rotenberg, A. Bostwick, and M. Grioni, *Consequences of Broken Translational Symmetry in FeSe_xTe_{1-x}*, Phys. Rev. Lett. **112**, 087602 (2014).

- [14] T. Hanaguri, S. Niitaka, K. Kuroki, and H. Takagi, *Unconventional s-wave superconductivity in Fe (Se, Te)*, *Science* **328**, 474 (2010).
- [15] I. I. Mazin and D. J. Singh, *Comment on "Unconventional s-wave superconductivity in Fe(Se,Te)"*, (2010), arXiv:1007.0047 [cond-mat.supr-con] .
- [16] T. Hanaguri, S. Niitaka, K. Kuroki, and H. Takagi, *Reply to comment on "Unconventional s-Wave Superconductivity in Fe(Se,Te)"*, (2010), arXiv:1007.0307 [cond-mat.supr-con] .

B

Appendix: Impurity states in Fe(Te,Se)

B.1. Anderson impurity in a (zero-bandwidth) BCS superconductor

We model the sub-surface impurity by an Anderson impurity embedded in a simple s -wave superconductor. The total Hamiltonian reads:

$$H_{\text{tot}} = H_S + H_T + H_{\text{IMP}}, \quad (\text{B.1})$$

where H_S is the Hamiltonian for the superconductor, H_T the tunneling contribution and H_{IMP} describes the impurity. In terms of fermion creation and annihilation operators for the superconductor (c) and the impurity level (d), each term is given by

$$H_S = \sum_{k,\sigma} \epsilon_k c_{k\sigma}^\dagger c_{k\sigma} + \sum_k (\Delta_s c_{k\uparrow}^\dagger c_{k\downarrow}^\dagger + \Delta_s^* c_{k\downarrow} c_{k\uparrow}), \quad (\text{B.2})$$

where Δ_s is the superconducting gap (here assumed to be real), and

$$H_T = \sum_{k,\sigma} t_s c_{k,\sigma}^\dagger d_\sigma + t_s^* d_\sigma^\dagger c_{k,\sigma}, \quad (\text{B.3})$$

where we take $t_s = \sqrt{\Gamma_s/\pi\nu_F}$ and ν_F is the density of states near the Fermi energy for $\Delta_s = 0$, which is taken to be constant.

$$H_{\text{IMP}} = \sum_\sigma \epsilon_0 d_\sigma^\dagger d_\sigma + U d_\uparrow^\dagger d_\downarrow^\dagger d_\downarrow, \quad (\text{B.4})$$

with U being the charging energy of the impurity.

In the normal state, this reduces to the standard Anderson model, including mixed-valence as well as Kondo physics below a characteristic Kondo temperature, T_K . In the superconducting state, this simplifies to a single Yu-Shiba-Rusinov (YSR) state, which can be tuned through zero energy by varying ϵ_0 , as long as $T_K \lesssim 0.3\Delta_s$ [1]. Here, we employ the zero-bandwidth approximation (ZBW), which replaces the superconductor by a single pair of BCS quasiparticles at the gap edge,

$$H_S^{\text{ZBW}} = \Delta_s c_\uparrow^\dagger c_\downarrow^\dagger + \Delta_s^* c_\downarrow c_\uparrow. \quad (\text{B.5})$$

From comparison with numerical renormalization group calculations, this approximation is known to capture the YSR states very well up to adjustments in the tunnel coupling, the value of which is fitted anyway [2].

In order to calculate the spectral weights of the impurity resonances in the Anderson model we use the Lehmann spectral representation of the Green's function. Using the many-body eigenstates $|n\rangle$ and the eigenenergies E_n of the ZBW Hamiltonian, the retarded Green's function on the impurity can be calculated as follows:

$$G_{\sigma\sigma'}^R(\omega) = \frac{1}{Z} \sum_{nn'} e^{-\beta E_n} \left(\frac{\langle n | d_\sigma | n' \rangle \langle n' | d_{\sigma'}^\dagger | n \rangle}{\omega + i\Gamma_r + E_n + E_{n'}} + \frac{\langle n | d_{\sigma'}^\dagger | n' \rangle \langle n' | d_\sigma | n \rangle}{\omega + i\Gamma_r + E_{n'} - E_n} \right), \quad (\text{B.6})$$

where $\beta = 1/(k_B T)$ and the partition function Z is given by $Z = \sum_n e^{-\beta E_n}$. Here we have included a phenomenological relaxation rate, Γ_r , which endows the otherwise sharp bound states by a finite lifetime broadening. The details of this quasiparticle relaxation time are beyond the scope of this work, but our analysis of the tunnelling current assumes it to be larger than or similar to the tip-impurity tunnelling rate, Γ_t . The local spectral function is expressed in terms of the impurity retarded Green's function as:

$$D_I(\omega, \epsilon_0) = -\frac{1}{\pi} \text{Im} \left[\sum_{\sigma} G_{\sigma\sigma}^R(\omega) \right]. \quad (\text{B.7})$$

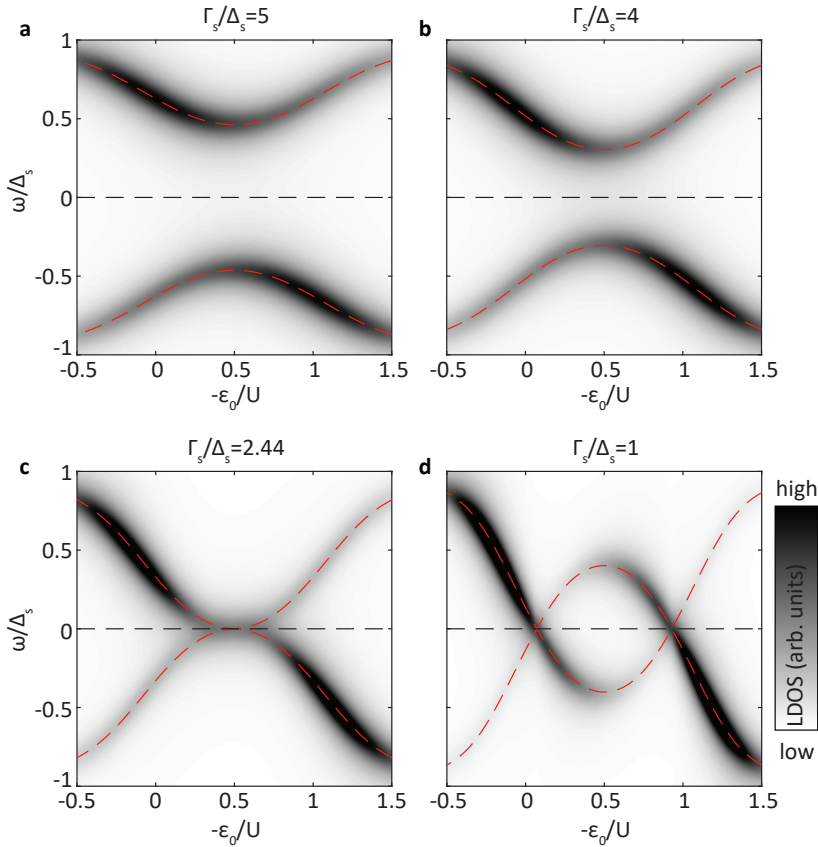


Figure B.1: **Local density of (sub-gap) states as a function of energy (ω) and impurity level energy (ϵ_0).** Different values of the tunnelling rate Γ_s are indicated on the top of each panel. The (YSR) bound state energy is highlighted with red dashed lines. In all panels we used $U/\Delta_s = 3$, together with a phenomenological quasiparticle relaxation rate, $\Gamma_r = 0.1\Delta_s$.

Figs. B.1 and B.2 show how this local density of (YSR) states changes with level energy, ϵ_0 , and tunnelling rate Γ_s , respectively. The quantum phase transition is

B

revealed as the point by which the YSR state crosses zero energy and the spectral weight is exchanged between positive, and negative energy states. This asymmetry in spectral weight has a simple origin within the ZBW model. The observed excitation is between a doublet state, which is simply a single electron on the dot ($|\uparrow_d, 0_{qp}\rangle, |\downarrow_d, 0_{qp}\rangle$), and a more complicated singlet state. This singlet state continuously evolves from an empty impurity level, $|0_d, 0_{qp}\rangle$, at $\epsilon_0/U \gg 0$ to a doubly occupied level, $|2_d, 0_{qp}\rangle$, at $\epsilon_0/U \ll -1$. In between, these two singlets are mixed with the YSR singlet, formed by the singly occupied impurity level and the single BCS quasiparticle doublet, i.e. $|\uparrow_d, \downarrow_{qp}\rangle - |\downarrow_d, \uparrow_{qp}\rangle$ states. As the positive (negative) part of the spectral function is related to excitations from adding an electron (hole) to the ground state, this part is largest for $\epsilon_0/U \gg 0$ ($\epsilon_0/U \ll -1$). Precisely at $\epsilon_0/U = -0.5$ the state is equally composed of empty and doubly occupied components and as such the spectrum shows no asymmetry. The larger Γ_s , the larger the gate-range around $\epsilon_0/U = -0.5$ in which the YSR singlet component dominates this excited singlet state, and the lower its energy. This explains both the closing of the doublet sector and the increased spectral symmetry as Γ_s/Δ_s increases, observed in Fig. B.1.

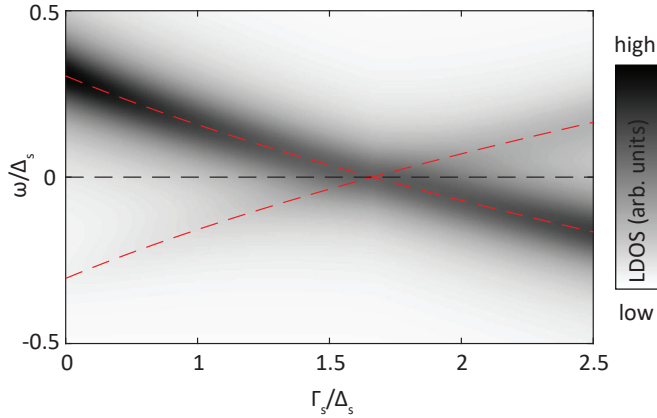


Figure B.2: **Local density of (sub-gap) states as a function of energy (ω) and tunneling rate (Γ_s).** The (YSR) bound state energy is highlighted with red dashed lines. For the simulations we used $U/\Delta_s = 3$, $\epsilon_0/\Delta_s = -2.5$, together with a phenomenological quasiparticle relaxation rate $\Gamma_r = 0.1\Delta_s$.

As is evident from these two figures, the phase transition may be induced either by tuning the level energy, ϵ_0 , or the tunnel coupling, t_s . As explained in 4, previous experiments [3] have reported a tip-induced tuning of t_s by assuming a force acting on the impurity from the tip. Whereas this seems feasible for a flexible molecule placed on the surface, we believe that this possibility is less likely in the present case, where the impurity is sub-surfactant. No indication of lattice deformation when tip-sample distance changes (pushing or pulling) is observed in our experiments. Therefore, we consider the effective gating mechanism much more likely to explain the observed tuning of the sub-gap states.

B.2. Azimuthally-averaged radial profiles and spatial mapping of the YSR resonances

For completeness in Figs. B.3a-e we present all the five azimuthally-averaged radial profiles, each at different tip-sample distance. In Fig. B.3f we also show a spatial map of the YSR resonances obtained by fitting a lorentzian.

B

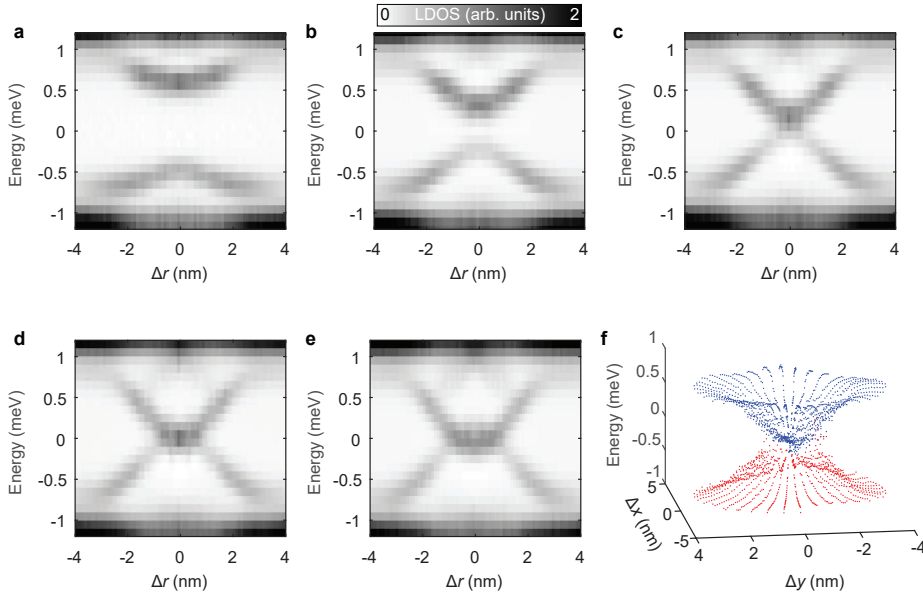


Figure B.3: **Azimuthally-averaged radial profiles and spatial mapping of the YSR resonances.** **a-e** Azimuthally-averaged radial cuts for $\Delta d(\text{\AA}) = 1.1, -0.2, -0.7, -1.2$ and -1.4 , respectively. Note that the colorbar applies to all panels. **f** Spatial mapping of the YSR energy resonances. The energy of each resonance is obtained by fitting a lorentzian at each point of LDOS(\mathbf{x}, ω) at $\Delta d(\text{\AA}) = -1.2$. Blue (red) dots represent the positive (negative) resonances.

B.3. Noise spectroscopy

As an extra verification for the performance of our junction, we used the Noise Scanning Tunneling Microscopy (NSTM) technique [4, 5] to measure the current noise as function of energy (noise spectroscopy) on a single location on the $\text{FeTe}_{0.55}\text{Se}_{0.45}$ surface, not at an impurity location, with the aim to look for the doubling of current noise due to Andreev reflections. Fig. B.4a shows the measured current noise power as function of applied bias $S(V)$, with the out of tunneling noise subtracted to remove the thermal noise component and input noise of the amplifier $S(V) - S(0)$. The dashed lines indicate the predicted shot noise curve [6–8] for tunneling of single electron charge (e) and double electron charge ($2e$). At a bias voltage larger than the superconducting gap energies, $eV > |\Delta_t + \Delta_s|$, the measured noise power data follows the predicted noise power for single electron tunneling. When the bias is lowered below the superconducting gap energies, $eV < |\Delta_t + \Delta_s|$, the current

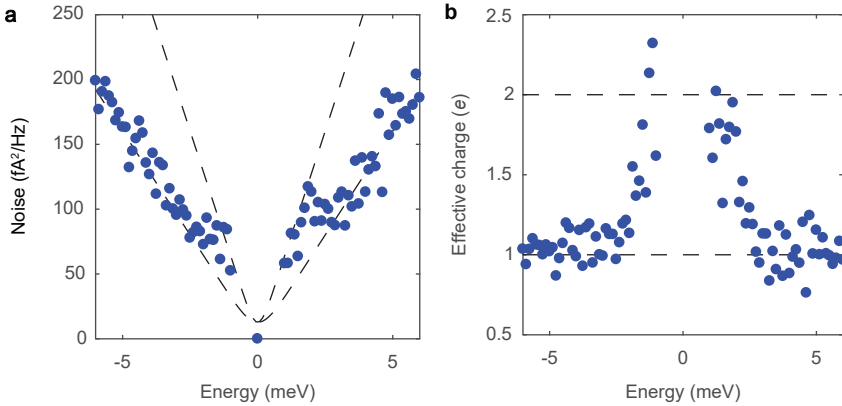


Figure B.4: **Shot-noise measurement on $\text{FeTe}_{0.55}\text{Se}_{0.45}$.** **a** Measured current noise power (blue dots) as function of applied bias on the $\text{FeTe}_{0.55}\text{Se}_{0.45}$ surface, while keeping a constant junction resistance of $R_N = 10 \text{ M}\Omega$. The black dashed lines represent the expected current noise power for $q = e$ and $q = 2e$ tunneling. **b** Effective charge (q) transferred between the Pb tip and $\text{FeTe}_{0.55}\text{Se}_{0.45}$ surface tunnel junction, obtained by dividing the measured current noise power by the full poissonian noise $2e|I|$, similar to the Fano factor. Dashed lines indicate $q = e$ and $q = 2e$.

noise clearly deviates from single electron charge transfer, showing a doubling of noise power to the $2e$ line, consistent with the appearance of Andreev reflection processes [7–9]. To show the effective charge transferred between the Pb tip and $\text{FeTe}_{0.55}\text{Se}_{0.45}$ surface we divide the measured noise power by the full Poissonian noise for single electron charge transport $S = 2e|I|$, which is shown in Fig. B.4b. This illustrates a clear step from e to $2e$ charge transfer when the bias is lowered below the superconducting gap energies $eV < |\Delta_t + \Delta_s|$, demonstrating that the tunneling current is now effectively carried by double charge quanta due to Andreev reflection processes that start to dominate. This is the first time such noise enhancement due to Andreev reflection processes is shown in a junction containing an unconventional superconducting electrode (the $\text{FeTe}_{0.55}\text{Se}_{0.45}$ surface), opening a potential new path for further investigation of the YSR or Majorana states by the means of noise spectroscopy.

B.4. Estimation of the potential drop in the vacuum barrier between tip and sample

In an STM experiment there is a potential drop in the vacuum tunneling barrier [10] due to the work function difference between tip (W_t) and sample (W_s), as illustrated in Fig. B.5a-c. As we explain in 4, this potential drop results into an effective electric field penetration in the sample which acts as a local gate. An estimation of the work function difference yields that in our experiment the tip has a larger work function than the sample. In more detail, we are using a Pt/Ir tip coated with Pb. From literature we find that the work functions are $W_{\text{Pt/Ir}} = 5 - 6 \text{ eV}$ and $W_{\text{Pb}} = 4.25 \text{ eV}$, respectively. This yields a rough estimation of the work

function of the tip $W_{\text{tip}} = 4.5 - 5$ eV. Concerning the top surface of our sample it consists of Se, $W_{\text{Se}} = 5.9$ eV and Te, $W_{\text{Te}} = 4.95$ eV atoms. However, previous STM experiments [11] show that Fe(Se,Te) has a significantly smaller work function of ~ 3 eV. This yields a work function difference of the order of 1 eV.

We note that a vertical movement of the tip has a stronger influence of the field at the impurity location than a horizontal movement because the radius of the apex of the tip is large compared to the tunneling distance, and because the electric field decays algebraically. This is illustrated in Fig. B.5d. The radius of the apex of typical STM tips is 10-100 nm. While the exact radius is unknown, we estimate it to be around 20 nm as the tip has been indented in Pb.

B

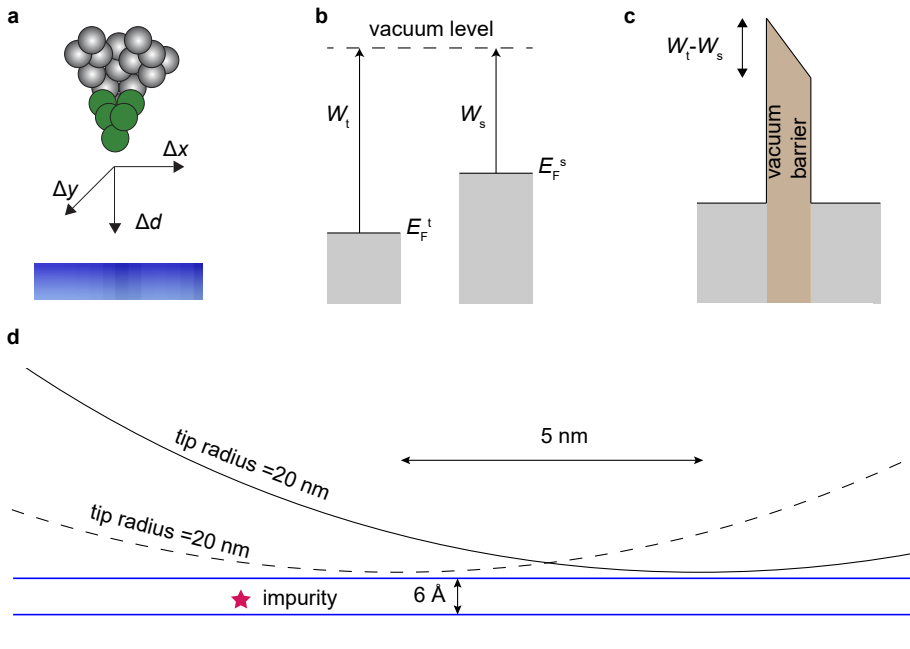


Figure B.5: **Potential drop in the vacuum barrier in an STM junction and tip-shape illustration.** **a** Schematic representation of the tip and sample. **b** Schematics of tip and sample density of states when they are isolated. Grey shaded areas indicate filled states whereas the work function is represented with arrows. **c** When a tunneling contact is formed due to the work function difference there is a potential drop in the vacuum barrier. **d** Tunneling junction schematics (in approximate scale). Two spherically shaped tips (radius is 20 nm) that are 5 nm apart are shown. An impurity resides below the surface (atomic planes are drawn as blue lines separated by 6 Å).

B.5. Estimation of the charging energy U of the impurity and the potential change on it due to the tip movement

B

Since we do not know the specific nature of the impurity, we make a rough estimate of its charging energy U by approximating the impurity orbital by a sphere of radius R . If the sphere already contains a single electron, the energy for placing the next will then be given by $U = e^2/(8\pi\epsilon_r\epsilon_0R)$, where ϵ_0 is the vacuum permittivity and ϵ_r the dielectric constant of the medium that the impurity is embedded. Assuming that $R = 1 - 3$ nm and $\epsilon_r \sim 15$ [12] we find that $U \sim 15 - 50$ meV. Next we want to show that when we move the STM tip closer to sample, we induce a potential shift on the impurity (which we assume that resides halfway between the topmost and the subsequent layer) that is comparable to the charging energy U , indicating that the gating scenario is possible. However, we emphasize that FeTe_{0.55}Se_{0.45} is an unconventional superconductor (e.g. low Fermi energy, inhomogeneous superfluid density). Hence, the simple calculation below for band-bending might not be applicable here and is therefore performed just for illustration purposes.

At first, we estimate the potential drop on the surface of the sample based on the image charges method which assumes that a spherical tip with radius r_t is in tunneling distance h from the sample. According to previous studies on semiconductors and correlated electron systems the voltage drop on the surface or band-bending potential V_{BB} is given by [10]

$$V_{\text{BB}} = \frac{1}{1 + \epsilon_r \frac{h}{r_t}} (V_b - W), \quad (\text{B.8})$$

here V_b is the bias voltage and W the work function difference between tip and sample ($W \sim 1$ eV and $V_b \sim 1$ meV in our experiments). Moreover, we chose $r_t = 20$ nm and $\epsilon_r = 15$ as explained before. As a last step, we employ the following exponential model to fit our conductance (G) versus Δd curve, for the estimation of the tip-sample distance h

$$G = G_0 e^{-2kh}. \quad (\text{B.9})$$

It is found that for the Δd tip movement shown in Fig. 4.3 the minimum (maximum) tip-sample distance is 2.9 (5.1) Å. This gives a change in the band-bending potential $\Delta V_{\text{BB}} \approx 0.1$ V on the surface.

Finally, the potential shift on the impurity is estimated by an exponential decay inside the bulk governed by the Thomas-Fermi screening length $\lambda_{\text{TF}} = 0.5$ nm, as calculated in the main text. That is

$$\Delta V_{\text{imp}} = \Delta V_{\text{BB}} e^{-d_{\text{imp}}/\lambda_{\text{TF}}}. \quad (\text{B.10})$$

For the impurity depth d_{imp} we choose 0.25 nm, resulting in $\Delta V = 60$ meV. From the simulations in Fig. 4.4 we found that when ϵ_0 changes by $\sim 0.1U = 2$ meV the YSR states disperse from the gap edge to zero-bias. Since our rough estimate shows that we can induce a larger change, we conclude that the gating scenario is possible.

B.6. Statistics

On one sample, we investigated 5 ring-shaped in-gap impurity features in a $45 \times 45 \text{ nm}^2$ field-of-view. All of them showed a dispersion when changing Δd and Δr . The dispersion in Δd is different in different impurities; the estimated cross of the YSR states at the Fermi level varies and is mostly below $\Delta d = -0.7 \text{ \AA}$. We did not measure all 5 impurities for smaller tip-sample distances but we expect similar X-shaped profiles. We assume that the different dispersions are due to their location inside the crystal. We can imagine that an impurity that is deeper in the crystal would be less prone to the influence of the electric field of the tip. On a second sample we found 2 additional impurity features extending over $\sim 4 \text{ nm}$. Note that we do not observe any impurities with robust zero-bias peaks that do not disperse.

References

- B**
- [1] J. Bauer, A. Oguri, and A. C. Hewson, *Spectral properties of locally correlated electrons in a Bardeen–Cooper–Schrieffer superconductor*, *J. Phys* **19**, 486211 (2007).
 - [2] K. Grove-Rasmussen, G. Steffensen, A. Jellinggaard, M. H. Madsen, R. Žitko, J. Paaske, and J. Nygård, *Yu-Shiba-Rusinov screening of spins in double quantum dots*, *Nat. Commun.* **9**, 2376 (2018).
 - [3] L. Farinacci, G. Ahmadi, G. Reecht, M. Ruby, N. Bogdanoff, O. Peters, B. W. Heinrich, F. von Oppen, and K. J. Franke, *Tuning the Coupling of an Individual Magnetic Impurity to a Superconductor: Quantum Phase Transition and Transport*, *Phys. Rev. Lett.* **121**, 196803 (2018).
 - [4] K. M. Bastiaans, T. Benschop, D. Chatzopoulos, D. Cho, Q. Dong, Y. Jin, and M. P. Allan, *Amplifier for scanning tunneling microscopy at MHz frequencies*, *Rev. Sci. Instrum.* **89**, 093709 (2018).
 - [5] K. M. Bastiaans, D. Cho, T. Benschop, I. Battisti, Y. Huang, M. S. Golden, Q. Dong, Y. Jin, J. Zaanen, and M. P. Allan, *Charge trapping and super-Poissonian noise centres in a cuprate superconductor*, *Nat. Phys.* **14**, 1183 (2018).
 - [6] Ya. M. Blanter and M. Büttiker, *Shot noise in mesoscopic conductors*, *Phys. Rep.* **336**, 1 (2000).
 - [7] M. J. M. de Jong and C. W. J. Beenakker, *Doubled shot noise in disordered normal-metal–superconductor junctions*, *Phys. Rev. B* **49**, 16070 (1994).
 - [8] J. C. Cuevas, A. Martín-Rodero, and A. L. Yeyati, *Shot Noise and Coherent Multiple Charge Transfer in Superconducting Quantum Point Contacts*, *Phys. Rev. Lett.* **82**, 4086 (1999).
 - [9] K. M. Bastiaans, D. Cho, D. Chatzopoulos, M. Leeuwenhoek, C. Koks, and M. P. Allan, *Imaging doubled shot noise in a Josephson scanning tunneling microscope*, *Phys. Rev. B* **100**, 104506 (2019).
 - [10] I. Battisti, V. Fedoseev, K. M. Bastiaans, A. de la Torre, R. S. Perry, F. Baumberger, and M. P. Allan, *Poor electronic screening in lightly doped Mott insulators observed with scanning tunneling microscopy*, *Phys. Rev. B* **95**, 235141 (2017).
 - [11] F. Masee, *A Tunnelers View on Correlated Oxides and Iron Based Superconductors*, *PhD thesis*, (2011).
 - [12] W. Zhao, M. Li, C.-Z. Chang, J. Jiang, L. Wu, C. Liu, J. S. Moodera, Y. Zhu, and M. H. W. Chan, *Direct imaging of electron transfer and its influence on superconducting pairing at FeSe/SrTiO₃ interface*, *Sci. Adv.* **4**, eaao2682 (2018).

C

Appendix: Noise above T_C in a disordered superconductor

C.1. STM measurement schematics and topography of TiN surface

Figure C.1 shows a measurement schematic and the topography of the TiN samples that we studied. TiN samples grown on Si substrates are glued using silver epoxy on a STM sample holder. The top TiN layer is electrically contacted by using silver epoxy as well, as illustrated in Fig. C.1a. Two- and three-dimensional topographic images of the scanned TiN surface are shown in Figs. C.1b and c, respectively. The observed topographic height variations are consistent with previously reported ones [1, 2].

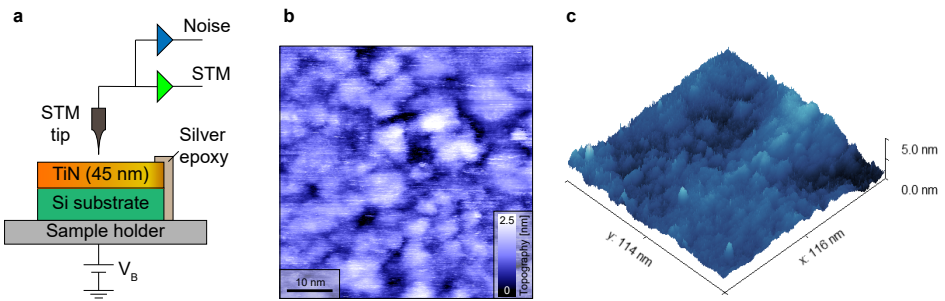


Figure C.1: **Measurement schematics and TiN topography.** **a** STM measurement schematic. **b** Topography of TiN. **c** Three-dimensional view of the TiN topography. The topography in **b** is obtained from a cropped area of the larger topograph in **c**. Setup conditions: $V_{\text{bias}} = 5 \text{ mV}$, $I_{\text{set}} = 100 \text{ pA}$.

C.2. Atomic layer deposited (ALD) TiN film

The 45 nm thick ALD titanium nitride film was grown on a Si substrate using plasma-assisted atomic layer deposition in an Oxford Instruments reaction chamber. The precursor TiCl_4 and a plasma of H_2 and N_2 are stepwise repetitively introduced and react into TiN and gaseous HCl, which is a self-limiting process. After each step, the residual gas is removed from the reaction chamber by an argon gas purge. During the deposition, the substrate is heated to 400 degrees Celsius and the plasma power is 400 W. More details on this sample can be found in Ref. [3].

C.3. Deposition of the sputtered TiN film

The sputtered film is deposited by reactive sputtering in a Trikon Sigma DC magnetron reactor. The 60 nm thick film is sputtered from a titanium target in a nitrogen/argon atmosphere (70/20 sccm) at room temperature and with a sputtering power of 6 kW onto a Si substrate, which is cleaned with an HF dip prior to deposition.

C.4. Error bars on excess noise

Error bars on the excess noise figures are determined by recording the fluctuations of the measured noise in time, and by estimating temperature fluctuations that have an influence on the thermal noise of the junction. The fluctuations of the measured noise in time are determined by time traces of the noise at constant bias at base temperature (Fig. C.2, measured noise at $R_J = 2.5 \text{ M}\Omega$ and $T = 2.5 \text{ K}$ for two different biases in tunneling and tip retracted (0 meV)). We then extract the standard deviation of these time traces and use it as the errorbar for our noise measurements, Fig. 6.2a and Fig. 6.3a. The temperature fluctuations are determined by logging the temperature at 7.2 K over a few days. We use the procedure described above, in order to propagate the errors of the excess noise to the effective charge versus energy plots.

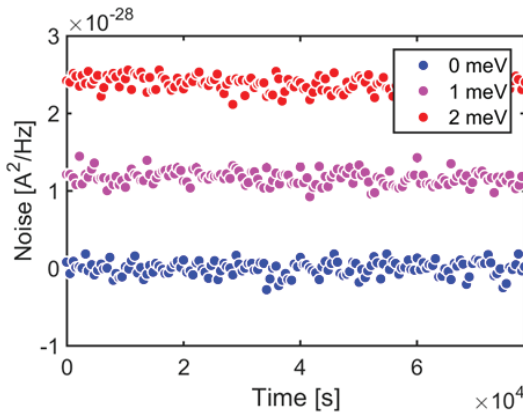


Figure C.2: **Noise time traces.** Time traces of noise at $R_J = 2.5 \text{ M}\Omega$ and $T = 2.5 \text{ K}$ for 0 meV (with the tip retracted), 1 meV and 2 meV energy. The average standard deviation of these time traces yields an error for the noise figures.

C.5. Transport measurements

Transport measurements were performed on TiN samples ($4.5 \text{ mm} \times 2.5 \text{ mm}$) glued on a chip carrier using Epotek H20E silver-epoxy and wire-bonded to the chip carrier to make a four-probe contact. Resistance versus temperature $R(T)$ (Fig. 6.4c) curves are measured using the four-probe method in a pulse tube cryostat with a base temperature of 1.5 K. The $R(T)$ curve (Fig. C.3) shows a so-called N-shaped curvature as it is typical for disordered superconductors not too close to the superconductor-insulator transition, as well as for some cuprate high-temperature superconductors, and which have been used to distinguish the different transport regimes. We observe two distinct features in the $R(T)$ curve: First, a local minimum interpreted as the 3D-2D crossover. Second, a local maximum (indicated with T_{max}) around 11.4 K; a signature that has been interpreted as the onset of superconducting fluctuations.

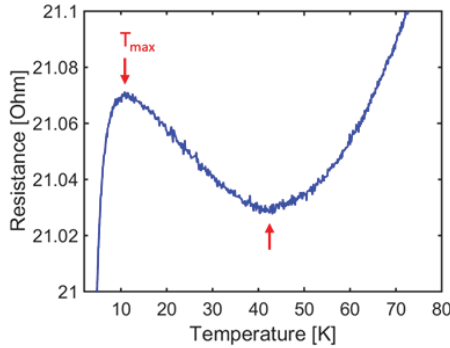


Figure C.3: **Detail of $R(T)$ curve.** The characteristic N-shaped curvature of $R(T)$ above T_C can be used to distinguish different transport regimes. The local minimum (lower red arrow) indicates the 3D-2D crossover. The local maximum (indicated with T_{\max}) gives the onset temperature below which transport is governed by superconducting fluctuations.

C.6. Spatial variations of the spectral gap

Differential conductance maps for both ALD grown and sputtered samples were measured in order to record the spatial variations of the spectral gap of TiN. Figs. C.4a and b show an intensity plot and histogram of the gap variations in a $50 \text{ nm} \times 50 \text{ nm}$ area at 2.2 K for the ALD-grown sample. The spectral gap is extracted by minimization of the second derivative of the measured differential conductance spectrum with respect to energy at each location. We find a mean gap of 1.78 meV with a standard deviation of 0.63 meV, which corresponds to $\sim 36 \%$ gap variations. The gap variations in our sample are similar to previously reported ones on 50 nm-thick sputtered TiN films [2]. Compared to thinner films (3.6 nm, Ref. [4]) our gap variations are significantly larger. Similarly for the sputtered sample (Fig. C.4c and d) we extract the gap variations in the same way to find a mean of 0.85 meV and a standard deviation of 0.11 meV corresponding to $\sim 13 \%$ gap variations.

C.7. Influence of thermal broadening and conventional Andreev reflections on the filling of the spectral gap

In Fig. C.55 we show that thermal broadening and conventional Andreev reflection cannot cause the filling of the spectral gap as shown in Fig. 6.4a. We start with density of states from Dynes formula representing a simple s-wave BCS gap with a fixed size of 1.78 meV for all temperatures,

$$N(E, \Gamma, \Delta) = \left| \operatorname{Re} \frac{E + i\Gamma}{\sqrt{(E + i\Gamma)^2 - \Delta^2}} \right|, \quad (\text{C.1})$$

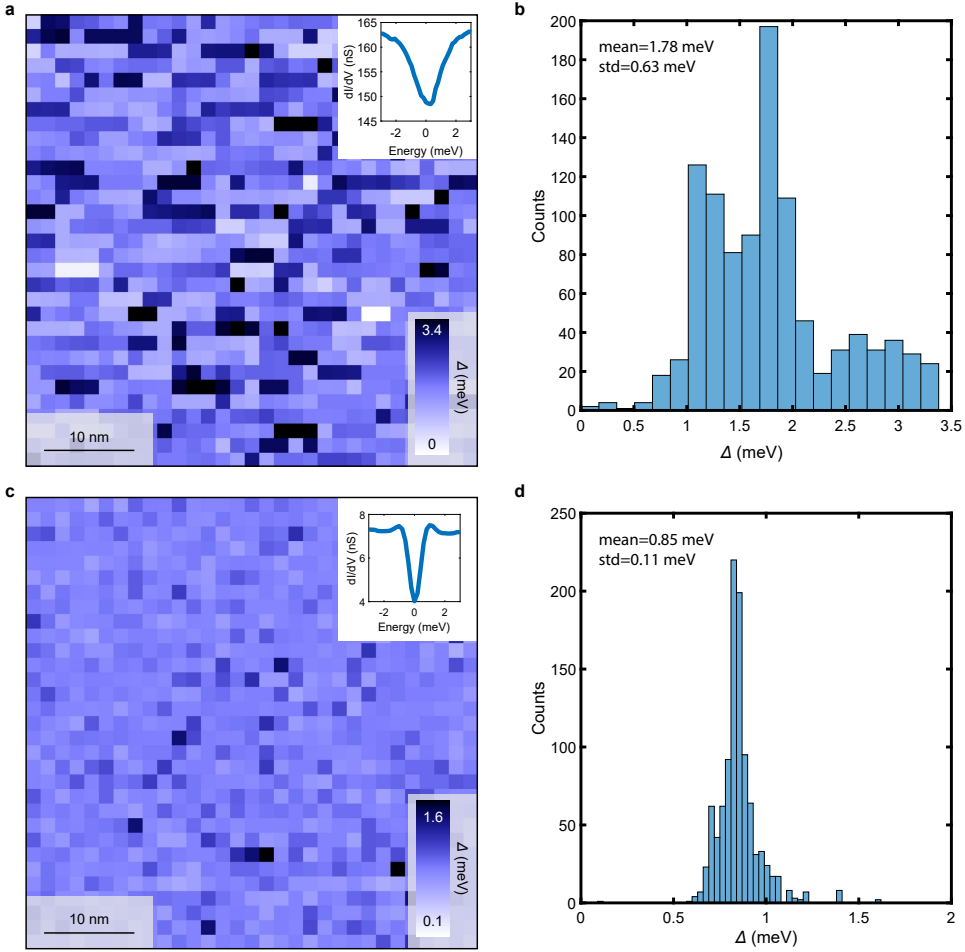


Figure C.4: **Mapping the spectral gap of TiN.** **a** Map of the spectral gap of TiN (grown by ALD) in a $50 \text{ nm} \times 50 \text{ nm}$ area at 2.2 K. Inset: average spectrum of the dI/dV spectra in the area. **b** Histogram of the gap values in **a**. A mean gap of 1.78 meV is observed and a standard deviation of 0.63 meV. **c** Same as in **a** for the TiN sample that was grown via sputtering. **d**. Same as in **b** for the TiN sputtered sample. A mean of 0.85 meV and standard deviation of 0.11 meV is observed.

and simulate integrated differential conductance assuming a constant density of states for the tip

$$g(V, T) = \int_{-\infty}^{+\infty} N(E, \Gamma, \Delta) \left[-\frac{\partial f(E + eV, T)}{\partial V} \right] t(E) dE, \quad (\text{C.2})$$

where $t(E)$ is tunneling probability and $f(E, T)$ is the Fermi–Dirac distribution at temperature T . The resulting filling of the gap due to thermally excited quasiparticles only contribute to up to 22% of the normal state conductance in the gap at

7.2 K. However, as shown in Fig. C.5c, even at 2.2 K the spectral gap is 91% filled.

We further include conventional Andreev reflection in the density of states (equivalent to the $T=0$ K line with two small peaks in Fig. C.5b), in the form of a pair of Lorentzian functions centred at ± 0.9 meV with an amplitude same as $\max[N(E, \Gamma, \Delta)]$ as an example. As described in the main text, Andreev processes occur with probability t^2 , while single electron tunneling occurs with probability t , where t is the transparency of the barrier. For the extreme case of $t = 10^{-2}$, the contribution of Andreev process to in-gap conductance is still negligible at our measuring temperature above 2.2 K. Therefore, we conclude that thermal broadening and conventional Andreev reflections cannot account for the filling of the spectral gap.

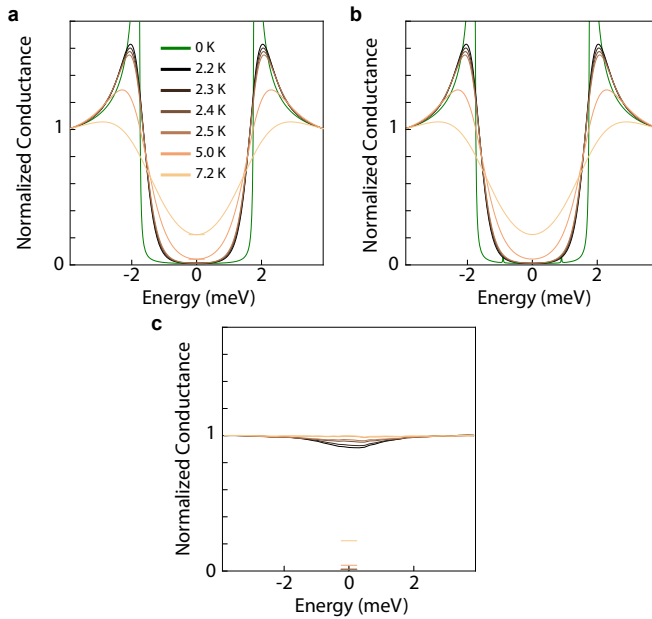


Figure C.5: **Filling of the spectral gap due to thermal broadening and conventional Andreev reflections.** **a** Simulation of normalized differential conductance as a function of energy at various temperatures for an s-wave BCS superconductor with a constant gap size $\Delta=1.78$ meV. **b** Same as **a** except two peaks inside the gap representing Andreev reflections are included in the zero-temperature density of states with barrier transparency of the tunnel junction $t = 10^{-2}$. **c** Normalized differential conductance data from Fig. 6.4a. The horizontal bars show contribution to filling of the spectral gap by thermal broadening and Andreev reflections for different temperatures.

C.8. Effect of temperature on the sharpness of the noise enhancement

In the main text we use a simple phenomenological Fermi function as a guide to the eye to the data (blue lines in Fig. 6.2 and Fig. 6.3) to include the effect of temperature on the step from $1e$ to $2e$. The reason that the noise does not rise immediately at Δ , but at energies just below Δ is based on a scattering matrix formalism model

that we will describe below for comparison, either model gives similar $S(V)$ curves, as shown in Fig. C.6. We calculate the current and the current noise in a normal metal – insulator – superconductor (NIS) junction using the reflection matrix with electron-hole grading of excitations at energy ϵ , adapted from the scattering matrix formalism of Refs [5, 6]:

$$r(\epsilon) = \begin{pmatrix} r_{ee}(\epsilon) & r_{eh}(\epsilon) \\ r_{he}(\epsilon) & r_{ee}(\epsilon) \end{pmatrix} \quad (\text{C.3})$$

The tunneling barrier is described by a normal scattering matrix for electrons,

$$\hat{S} = \begin{pmatrix} \rho & \tau \\ \tau & \rho' \end{pmatrix} \quad (\text{C.4})$$

with the transmission $|\tau|^2 = t$ and $\rho' = -\rho^* \tau / \tau^*$ assumed to be energy independent. Current conservation implies that the scattering matrix \hat{S} is an unitary matrix ($\hat{S}^* \hat{S} = \hat{S} \hat{S}^* = 1$), thus $|\tau|^2 + |\rho|^2 = 1$. The corresponding matrix for holes is \hat{S}^* . The N-S interface is described by the Andreev reflection amplitude $a(\epsilon)$ given by

$$a(\epsilon) = \frac{1}{\Delta} \begin{cases} \epsilon - \text{sgn}(\epsilon) \sqrt{\epsilon^2 - \Delta^2} & \text{for } |\epsilon| > \Delta \\ \epsilon - i \sqrt{\Delta^2 - \epsilon^2} & \text{for } |\epsilon| < \Delta \end{cases} \quad (\text{C.5})$$

where Δ is the magnitude of the pair-breaking gap. The reflection amplitudes $r_{ee}(\epsilon)$ and $r_{he}(\epsilon)$ in the scattering matrix can be found from an infinite series expansion for all possible electron and hole trajectories in the junction. By taking the distance between the N-S interface to zero, one can approximate these infinite series by:

$$r_{ee}(\epsilon) = \rho + \frac{\tau^2 \rho'^* a^2(\epsilon)}{1 - |\rho|^2 a^2(\epsilon)}, \quad (\text{C.6})$$

and

$$r_{he}(\epsilon) = \frac{\tau^2 a(\epsilon)}{1 - |\rho|^2 a^2(\epsilon)}. \quad (\text{C.7})$$

In order to calculate the current and current noise we use the expectation amplitudes for these reflections $R_{ee}(\epsilon) = |r_{ee}(\epsilon)|^2$ and $R_{he}(\epsilon) = |r_{he}(\epsilon)|^2$. The current is obtained by

$$I = \frac{2e^2}{h} \int_0^{eV} d\epsilon [1 - R_{ee}(\epsilon) - R_{he}(\epsilon)] [f(\epsilon - eV) - f(\epsilon)] \quad (\text{C.8})$$

where e is the elementary charge, h is Planck's constant, V is the applied bias voltage to the junction and we included the thermal resolution of the experiment by the Fermi-Dirac distribution $f(\epsilon) = 1/(1 + \exp(\epsilon/k_B T))$, where k_B is Boltzmann's constant and T is the temperature. The noise is found by

$$S_I = \frac{4e^2}{h} \int_0^{eV} d\epsilon [R_{ee}(\epsilon) - R_{ee}^2(\epsilon) + R_{he}(\epsilon) - R_{he}^2(\epsilon) + 2R_{ee}(\epsilon)R_{he}(\epsilon)] [f(\epsilon - eV) - f(\epsilon)] \quad (\text{C.9})$$

To simulate the effective charge transferred in the junction we calculate the ratio $S_I/2I$ for each bias voltage V . An example fit to the data is shown in Fig. C.6.

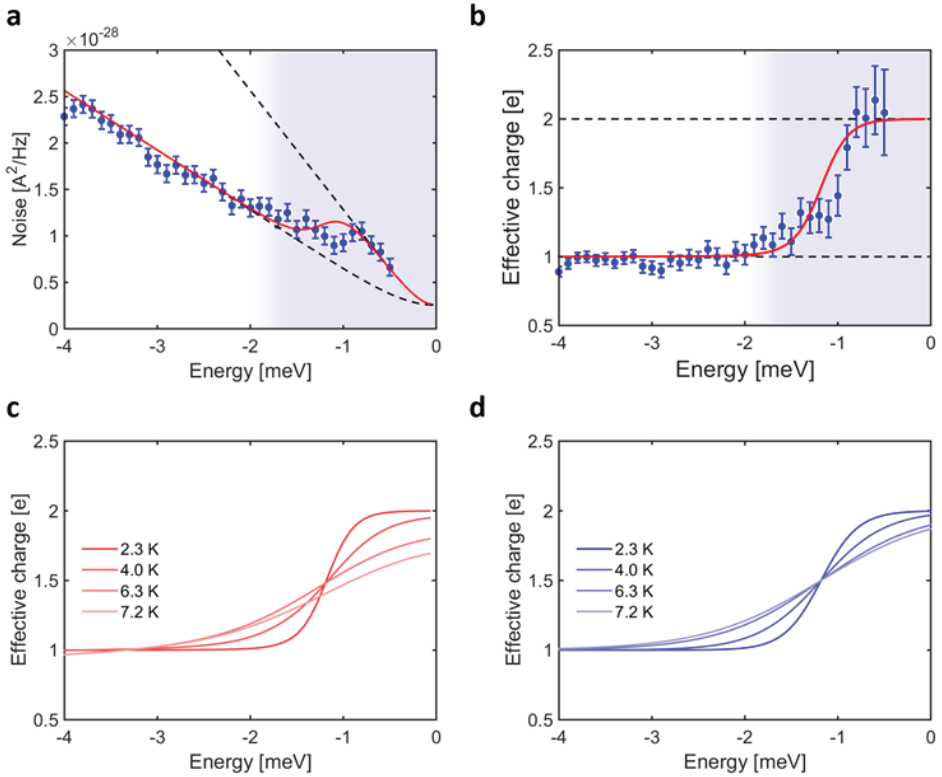


Figure C.6: **Random-scattering matrix fit to the noise data.** **a** The measured noise at 2.3 K as function of the bias voltage (blue dots) and random-scattering matrix simulation fit (red line). Blue shading indicates the spectral gap observed in the differential conductance. **b** Similar to **a** but now for the effective charge. **c** Random scattering matrix simulation for the four different temperatures used in the experiment. **d** Guides to the eye used in the main text.

References

- [1] C. Chapelier, W. Escoffier, B. Sacépé, J. C. Villégier, and M. Sanquer, *Scanning tunneling spectroscopy on a disordered superconductor*, AIP Conference Proceedings **850**, 975 (2006).
- [2] W.-T. Liao, T. P. Kohler, K. D. Osborn, R. E. Butera, C. J. Lobb, F. C. Wellstood, and M. Dreyer, *Scanning tunneling Andreev microscopy of titanium nitride thin films*, Phys. Rev. B **100**, 214505 (2019).
- [3] E. F. C. Driessen, P. C. J. J. Coumou, R. R. Tromp, P. J. de Visser, and T. M. Klapwijk, *Strongly Disordered TiN and NbTiN *s*-Wave Superconductors Probed by Microwave Electrodynamics*, Phys. Rev. Lett. **109**, 107003 (2012).
- [4] B. Sacépé, C. Chapelier, T. I. Baturina, V. M. Vinokur, M. R. Baklanov, and M. Sanquer, *Disorder-induced inhomogeneities of the superconducting state*

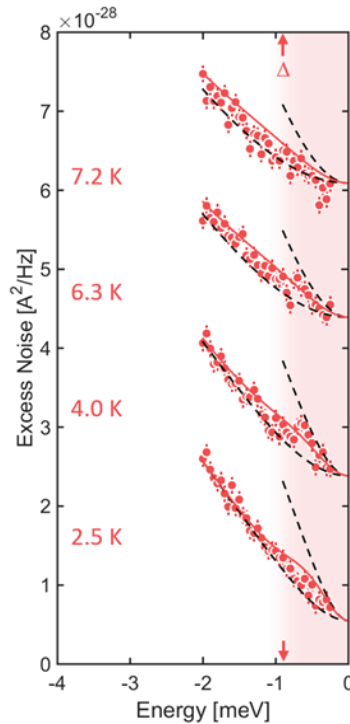


Figure C.7: **Enhanced noise above T_C for the sputtered sample.** Noise spectroscopy on sputtered TiN sample for varying temperatures 2.5 K to 7.2 K. Red dots indicate the measured excess noise in the junction as function of bias voltage at a junction resistance of $R_J = 2.5 \text{ M}\Omega$. The different temperature curves are offset for clarity. Dashed lines indicate the expected noise for $q^* = 1e$ and $q^* = 2e$. Red shading highlights the spectral gap measured in the differential conductance.

close to the superconductor-insulator transition, Phys. Rev. Lett. **101**, 157006 (2008).

- [5] C. W. J. Beenakker, *Random-matrix theory of quantum transport*, Rev. Mod. Phys. **69**, 731 (1997).
- [6] Y. Ronen, Y. Cohen, J.-H. Kang, A. Haim, M.-T. Rieder, M. Heiblum, D. Mahalu, and H. Shtrikman, *Charge of a quasiparticle in a superconductor*, PNAS **113**, 1743 (2016).

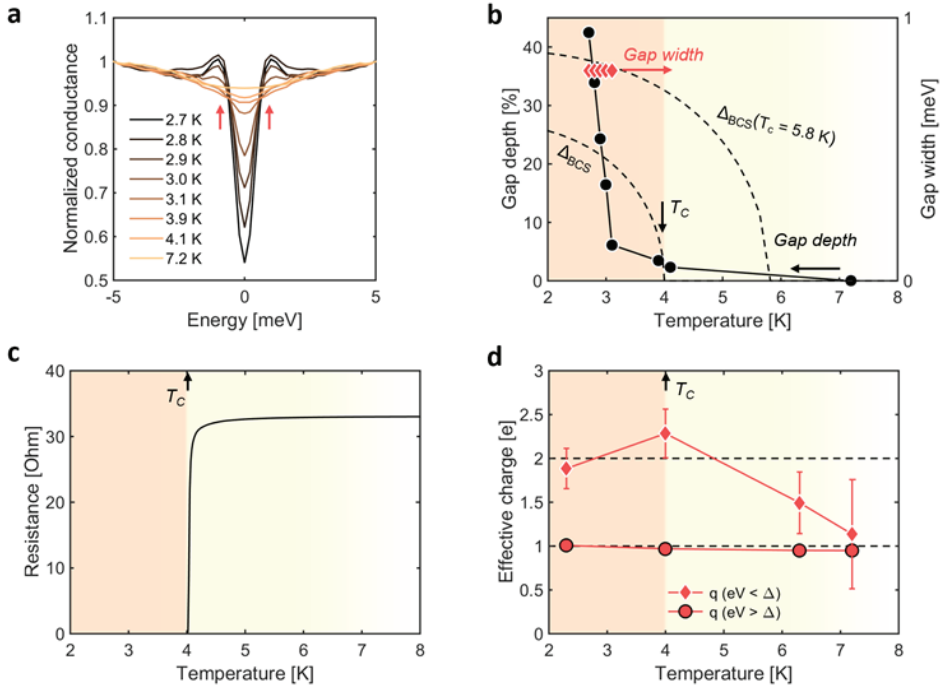


Figure C.8: **Evidence for a preformed-pair phase above T_C for the sputtered sample.** **a** Temperature dependence of the spectral density gap measured by the differential tunneling conductance between 2.7 K and 7.2 K. Red arrows indicate the gap width below T_C determined by minimum of second derivative. Setup conditions: $V_{bias} = 2 \text{ mV}$, $I_{set} = 200 \text{ pA}$. **b** Gap width (red diamonds) determined via the second derivative of the curves in panel **a**. The dashed curves indicates the mean-field prediction for $\Delta(T_C = 4 \text{ K})$ and $\Delta(T_C = 5.8 \text{ K})$ from BCS theory. The depth of the gap at zero bias (black dots) for the curves in panel **a** is shown in percentages with respect to the conductance at energies outside the gap. **c** Resistance versus temperature curve of our sputtered TiN sample. The orange shaded region indicates the phase-coherent superconducting phase below the transition temperature. **d** Effective charge outside (diamonds) and inside (circles) the spectral gap as function of temperature. We define the temperature T_p at the drop of the noise.

List of Publications

5. Koen M. Bastiaans, **Damianos Chatzopoulos**, Jian-Feng Ge, Doohee Cho, Willem O. Tromp, Jan M. van Ruitenbeek, Mark H. Fischer, Pieter J. de Visser, David J. Thoen, Eduard F. C. Driessen, Teunis M. Klapwijk, Milan P. Allan, *Direct evidence for Cooper pairing without a spectral gap in a disordered superconductor above T_C* , arxiv:2101.08535 (2021).
4. **Damianos Chatzopoulos***, Doohee Cho*, Koen M. Bastiaans*, Gorm O. Steffensen, Damian Bouwmeester, Alireza Akbari, Genda Gu, Jens Paaske, Brian M. Andersen, Milan P. Allan, *Spatially dispersing Yu-Shiba-Rusinov states in the unconventional superconductor $\text{FeTe}_{0.55}\text{Se}_{0.45}$* , Nature Communications **12**, 298 (2021).
3. Doohee Cho*, K. M. Bastiaans*, **Damianos Chatzopoulos***, Genda Gu, Milan P. Allan, *A strongly inhomogeneous superfluid in an iron-based superconductor*, Nature **571**, 541-545 (2019).
2. K. M. Bastiaans, Doohee Cho, **Damianos Chatzopoulos**, Maarten Leeuwenhoek, Corne Koks, and Milan P. Allan, *Imaging doubled shot noise in a Josephson scanning tunneling microscope*, Physical Review B **100**, 104506 (2019).
1. K. M. Bastiaans, Tjerk Benschop, **Damianos Chatzopoulos**, Doohee Cho, Quan Dong, Yong Jin, Milan P. Allan, *Amplifier for scanning tunneling microscopy at MHz frequencies*, Review of Scientific Instruments **89**, 093709 (2018).

Curriculum Vitæ

Damianos Chatzopoulos

12-08-1992 Born in Heraklion, Crete, Greece.

Education

- 2007–2010 High School
11th High school of Heraklion, Crete, Greece
- 2010–2015 Bachelor of Science in Physics
National & Kapodistrian University of Athens, Athens, Greece
Thesis: *"Mid-IR Quantum Cascade Lasers"*
supervised by Prof. D. Syvridis
- 2015–2017 Master of Science in Applied Physics
Technical University of Delft, Delft, The Netherlands
Thesis: *"Superconducting nanodevices for single-molecule transport studies: Experiments and Simulations"*
supervised by Prof. H. S. J. van der Zant
- 2017–2021 Doctor of Philosophy in Physics
Leiden University, Leiden, The Netherlands
Thesis: *"Josephson and noise scanning tunneling microscopy on conventional, unconventional and disordered superconductors"*
supervised by Dr. M. P. Allan

Acknowledgements

First of all, I would like to thank Milan Allan for giving me the chance to work in his young and dynamic group in Leiden University. Milan, I really enjoyed your guidance throughout the past four years and all those physics discussions we had on a daily basis. It has been a great experience performing research in your lab! In addition, thank you for urging me to participate in conferences and schools. It was a great pleasure to be given the opportunity to travel around the globe in order to present our research and broaden this way my research horizons.

Next, I would like to express my sincere acknowledgements to Jan Aarts for his willingness to be the promotor of this PhD thesis and for his input in my annual review meetings.

I would also like to thank the members of the examining committee of this thesis for taking the time to read it and evaluate it. In particular I thank Benjamin Sacepe, Nandine Hauptmann, Sense Jan van der Molen, Jan van Ruitenbeek and Eric Eliel.

Next, I thank Koen Bastiaans and Doohee Cho for the excellent collaboration throughout all these years. Thanks guys for introducing me to the STM techniques, the countless physics discussions and your patience.

The noise simulations presented in chapter 2 of this thesis were performed in close collaboration with Hermann Grabert, who is greatly acknowledged for his time and effort.

During the work of chapter 4 of the thesis I enjoyed external collaboration with Jens Paaske, Brian Andersen, Gorm Steffensen, Damian Bouwmeester, Genda Gu and Alireza Akbari. I would like to thank all of them for their contribution to the understanding of these peculiar states in Fe(Te,Se) and for the collaboration.

Chapter 6 of this thesis is a result of a fruitful collaboration with Mark H. Fischer, Pieter J. de Visser, David J. Thoen, Eduard F.C. Driessen and Teunis M. Klapwijk. They are all acknowledged for providing us with high-quality samples as well as for giving useful insights towards the understanding of our experimental observations.

At this point I would like to thank the people in Delft University that I worked with during my Master's thesis: Herre van der Zant and Joeri de Bruickjere. It was an amazing experience working with you that helped shape my research ideas.

Working in the Allan lab has been an amazing endeavour, among others, because of the friendly atmosphere created by its former and current members. Irene Battisti, Maarten Leuwenhoek, Tjerk Benschop, Willem Tromp, Vincent Stalman, Jacky Ge, Jiassen Niu, Jinwon Lee. Thank you for the everyday interaction! It has been a great pleasure!

Interaction with people outside our lab was equally enjoyable. The following people from the physics department at Leiden university are acknowledged for creating a great atmosphere in the department, key for the everyday life in the insti-

tute: Norman Blumel, Aymen Ben Hamida, Remko Fermin, Marcel Hesselberth, Tobias de Jong, Martin de Wit, Kaveh Lahabi, Paul Logman, Koen van Deelen, Wolfgang Loffler, Tjerk Oosterkamp, Michel Orrit, Tim Fuchs, Deep Punj, Douwe Scholma, Jedrej Tepper, Jelmer Wagenaar and Gesa Welker.

The people working in the Fine Mechanical and the Electronics department are greatly acknowledged for their help with equipment. In particular I would like to thank, Gijsbert Verdoes, Kees van Oosten, Freek Groenewoud, Ruud van Egmond, Harmen van der Meer, Rene Overgaw, Ko Koning, Peter van Veldhuizen and Raymond Koeler for their help with small or big technical tasks.

Special acknowledgements go to Wilfred van der Geest. Low temperature STM requires liquid helium and for the past four years Wilfred has always been there by providing it. Equally important was the help of Ellie van Rijsewijk and Michele Wijfje with administration formalities. Ellie and Michele, thank you for all the help!

The cover of this thesis was designed by Maxim Houdijk, who I want to thank for taking the time to make this beautiful image. In addition, I thank Dimitra Soubry for the Dutch translation of the Summary! Bedankt Dimitra!

I want to thank my friends back in Greece (Kostis, Evi, Paschalis) and in Delft (Stamatis, Nicole, Enri, Angelos, Rodoula, Andre and Guan). Thanks for all those nice memories guys!

Last but not least, I would like to thank my family (mum, dad and the kid) for the constant support and for caring about me. And of course my Rose, thank you for all the love, patience and support. Off we go for new adventures!